
BA-T: An Iterative Transformer for Two-View Bundle Adjustment

Ganlin Zhang^{1,2} Weirong Chen^{1,2} Daniel Cremers^{1,2} Xi Wang^{1,2,3}
¹ TU Munich ² MCML ³ ETH Zurich

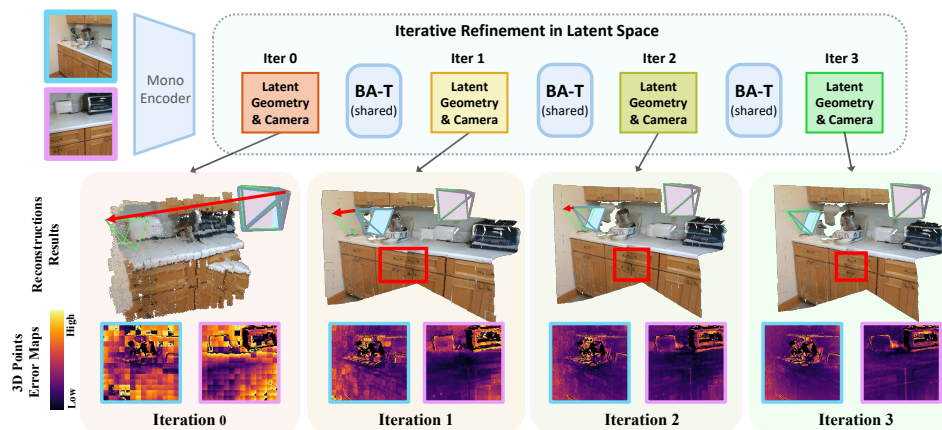


Figure 1: **Overview of BA-T.** Given input images, BA-T performs iterative updates on camera and local geometry tokens using a compact, reusable BA-T layer in latent space. \leftarrow indicates error between **GT poses** and estimated poses (**blue** and **pink**), which gradually decreases, and **red boxes** highlight regions progressively refined across iterations. The 3D point error maps visualize the per-view 3D point errors.

Abstract

Feed-forward models for 3D reconstruction have achieved strong performance using deep cross-view attention to exchange information across images. However, these approaches often depend on heavy decoder stacks and lack a structured mechanism for geometry refinement, resulting in poor multi-view consistency. We address this by drawing inspiration from classical bundle adjustment (BA), which can be viewed as an *iterative information propagation process* between poses and local geometry. Inspired by BA, we propose BA-T, an iterative Transformer that implements BA-style structured updates as a repeatable layer in implicit token space. Instead of relying on deep attention stacks, BA-T refines predictions based on latent residual by a single lightweight layer. Experiments demonstrate that BA-T progressively improves pose and reconstruction accuracy across iterations, achieves stronger cross-view consistency than conventional decoders, and matches or surpasses substantially larger models while using only 16% of their decoder parameters. BA-T provides a compact, efficient, and structural alternative to depth-heavy attention, enabling accurate 3D reconstruction within a lightweight architecture. The code will be made publicly at <https://github.com/zhangganlin/BA-T>.

1 Introduction

Estimating dense 3D structure and camera poses from multi-view images is fundamental in 3D computer vision, with applications in robotics, AR/VR, and autonomous driving. To obtain dense reconstructions, recent feed-forward methods [42, 18, 39, 17, 43, 19] directly regress dense 3D pointmaps (and camera poses) in a single forward pass. To enforce multi-view consistency, they use deep cross-view attention blocks as decoders to exchange information across images. While effective, these models rely on heavy decoder stacks to approximate geometric constraints and lack a mechanism to self-correct misalignments, limiting their robustness.

In contrast, classical bundle adjustment (BA) [37, 1, 2] refines camera poses and scene structure through iterative optimization, explicitly enforcing geometric consistency. However, its explicit geometric formulation makes it hard to embed in learning-based methods using implicit token representations. Recently, there are learning-based 3D reconstruction systems [33, 35, 36, 40] trying to incorporate differentiable BA modules into their pipelines to improve reconstruction accuracy by adjusting predicted feature correspondences or optical flow. Nevertheless, these BA components still operate as external optimization stages: predictions are first converted into *explicit geometric representations* (e.g., point clouds [33, 40] or feature tracks [35, 36]), after which explicit second-order solvers are applied. Although differentiable, this design still performs iterative updates on explicit geometry, limiting its ability to leverage the expressive power of latent representations. Related iterative refinement strategies operating directly on latent representations have been explored for 3DGS [44], but only for novel view synthesis rather than geometric reconstruction.

This reveals a key gap: feed-forward models leverage powerful latent token spaces but lack structured geometric refinement, while classical optimization is principled and iterative yet relies on explicit geometry, limiting integration with expressive latent representations. To bridge this gap, we draw inspiration from the *structured* iterative refinement of BA, where pose and geometry structure are progressively updated through repeated information propagation. Motivated by this, we propose **BA-T** (fig. 1), a BA-inspired iterative Transformer that mimics BA-style information flow through repeatable learnable updates directly in implicit token space.

BA-T replaces deep cross-view attention stacks with a single structured iterative refinement layer, enabling more compact and efficient updates of camera poses and 3D geometry than vanilla cross-attention blocks. By combining latent 3D representations, feed-forward efficiency, and BA-inspired self-consistency, it bridges end-to-end regression and iterative optimization. Experiments show that BA-T progressively improves pose and reconstruction accuracy, achieves stronger multi-view consistency than conventional decoder stacks, and matches or surpasses substantially larger models while using only 16% of DUS3R’s decoder parameters [42], showing that structured iterative refinement can replace depth-heavy attention while remaining lightweight and accurate.

In summary, our main **contributions** are as follows:

- We propose BA-T, a compact learnable, *bundle-adjustment-inspired* iterative Transformer layer for structured pose and geometry refinement.
- We refine relative camera poses and local geometry at the token level in an *implicit latent space*, leveraging the strong expressiveness of latent tokens.
- We achieve superior accuracy and multi-view consistency with a single *reusable* layer, outperforming conventional decoders relying on much deeper stacks while being more lightweight and computationally efficient.

2 Related Work

3D Reconstruction with Classical Bundle Adjustment. Classical 3D reconstruction systems [6] use bundle adjustment (BA) to jointly optimize camera poses and 3D structure through iterative refinement. Sparse feature-based methods [9, 29, 22, 24, 20] estimate camera trajectories and 3D points from keypoints, refining them by minimizing reprojection error via BA. In contrast, direct methods [13, 12, 14, 46, 45] optimize pixel intensities instead of sparse correspondences, formulating reconstruction as photometric error minimization. Dense extensions, such as DROID-SLAM [35] and others [15, 52, 50, 28, 51] integrate learned priors with differentiable bundle adjustment, achieving strong geometric consistency through iterative optimization that explicitly couples pose and structure variables. However, these approaches still rely on solver-based explicit

updates and require constructing and inverting large second-order Hessian matrices during inference. Such computational overhead makes seamless integration with modern large-scale feed-forward architectures challenging. Moreover, their dependence on optimization dynamics can limit robustness in texture-less or low co-visibility scenarios, where feed-forward models may instead benefit from large-scale data-driven priors.

3D Reconstruction with Feed-Forward Models. Recent learning-based methods perform geometry and pose estimation in a single forward pass. DUST3R [42] perform two-view reconstruction by regressing pointmaps in a shared global frame, while sequential extensions [38, 5, 41] propagate reconstructions across multiple frames. Two-view follow-ups [49, 26] predict local, view-dependent geometry for greater downstream flexibility. More recent models, including VGGT [39] and others [17, 43, 19], are trained on multi-view data to generalize across more views, and SLAM-Former [48] supports mixed inputs of reconstructed and new frames to enhance consistency. A common characteristic of these feed-forward methods is the heavy use of cross-view attention blocks as geometric decoders for cross-view information exchange. Geometric consistency is enforced implicitly through deep stacks of attention layers, requiring increasingly large and computationally intensive models to approximate the constraints that classical optimization enforces explicitly. Despite their depth and capacity, these models lack an iterative correction mechanism at inference time: once a forward pass is completed, prediction errors cannot be systematically refined.

In contrast, our proposed BA-T replaces heavy cross-view attention stacks with structured, repeatable refinement steps inspired by bundle adjustment. By embedding BA-inspired information propagation into a compact architecture, our method combines efficient feed-forward prediction with iterative geometric refinement without explicit solver-based optimization.

3 BA-T

3.1 Preliminary: Information Propagation of Bundle Adjustment

Bundle Adjustment (BA) jointly optimizes scene geometry and camera parameters by minimizing residuals through iterative refinement. In this process, information circulates between camera estimates and geometry estimates through repeated updates. Many BA variants exist, depending on the choice of residuals and the representation of geometry. We begin by presenting a general formulation of BA for the simplest two-view case. Given two images I_a and I_b , BA aims to optimize their local geometry $\mathbf{g}_a, \mathbf{g}_b$ and their relative camera pose c . Consider a pair of local regions (e.g., a pixel or a patch) $p \in I_a$ and $q \in I_b$. The local geometry associated with p , denoted by $g_a^p \in \mathbf{g}_a$, is transformed into the local space of I_b via the space transform function $\pi_c^{a \rightarrow b}(\cdot)$. A property f of the transformed local geometry is then compared with the corresponding measurement using a *residual function* $r(\cdot, \cdot)$, which forms the core objective of bundle adjustment. The resulting optimization problem can be written as

$$\hat{c}, \hat{\mathbf{g}}_a, \hat{\mathbf{g}}_b = \min_{c, \mathbf{g}_a, \mathbf{g}_b} \left(\sum_{p \in I_a, q \in I_b} r(f(g_b^q), f(\pi_c^{a \rightarrow b}(g_a^p))) \right), \quad (1)$$

To solve the optimization problem, the classical way uses a second-order Gauss-Newton solver [23], taking use of the Jacobian matrix \mathbf{J}_c and \mathbf{J}_g :

$$\begin{bmatrix} \mathbf{J}_c^T \mathbf{J}_c & \mathbf{J}_c^T \mathbf{J}_g \\ \mathbf{J}_g^T \mathbf{J}_c & \mathbf{J}_g^T \mathbf{J}_g \end{bmatrix} \begin{bmatrix} \Delta c \\ \Delta g \end{bmatrix} = - \begin{bmatrix} \mathbf{J}_c^T \\ \mathbf{J}_g^T \end{bmatrix} r \xrightarrow{\text{rewrite as}} \begin{bmatrix} \mathbf{B} & \mathbf{E} \\ \mathbf{E}^T & \mathbf{C} \end{bmatrix} \begin{bmatrix} \Delta c \\ \Delta g \end{bmatrix} = \begin{bmatrix} \mathbf{v} \\ \mathbf{w} \end{bmatrix}, \quad (2)$$

and the update Δc and Δg can be solved by Schur Complement [16]:

$$\Delta c = [\mathbf{B} - \mathbf{E}\mathbf{C}^{-1}\mathbf{E}^T]^{-1} (\mathbf{v} - \mathbf{E}\mathbf{C}^{-1}\mathbf{w}), \quad \Delta g = \mathbf{C}^{-1}(\mathbf{w} - \mathbf{E}^T\Delta c). \quad (3)$$

These equations summarize the information flow in BA: residuals are first computed, the camera update aggregates the coupled residual information through the Schur complement, and the resulting camera change is then used to refine the geometry.

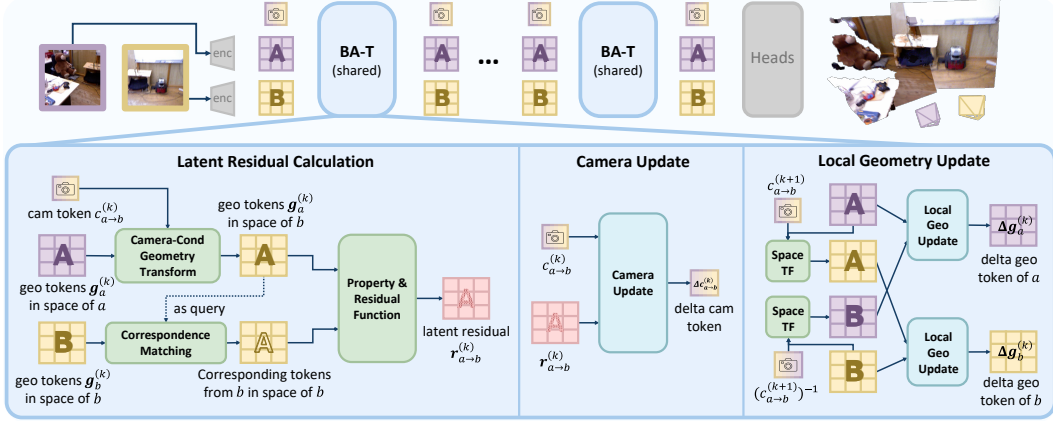


Figure 2: **Overview of the BA-T pipeline.** BA-T takes camera tokens (from learnable initialization) and local geometry tokens (from the image encoder) as input and refines them iteratively. At each step, it performs a BA-inspired implicit refinement step by transforming geometry tokens across camera spaces, matching correspondences, and computing latent residuals. Camera tokens and per-view geometry tokens are refined via the Camera Update and Local Geometry Update respectively.

3.2 Method Overview: BA-inspired Transformer for Implicit Refinement

Notation. Single-token variables or functions are denoted by normal t , multi-token ones by bold \mathbf{t} , and iteration indices by superscripts, $t^{(k)}$.

BA-T. Classical BA explicitly constructs and solves the normal equations (eq. (2)) via iterative second-order optimization, providing strong geometric guarantees but relying on explicit geometry, hand-crafted residuals, Jacobians, and large matrix inversions, making it difficult to integrate into modern end-to-end learning frameworks or scale to latent implicit representations.

The update equations eq. (3) already reveal the key pattern we want to preserve: information flows back and forth between camera and geometry through repeated refinement. Rather than explicitly forming and solving linear systems, we take this *iterative information propagation* of BA as a design cue for a learnable refinement layer between camera parameters and local geometry. This dependency structure can be seen as a global information flow, where updates to one set of variables propagate and influence the other, motivating a learnable mechanism that emulates this interaction pattern.

We model this pattern of information propagation with a learnable layer, **BA-T** (fig. 2), treating camera and geometry parameters as latent tokens, and use attention layers to learn the interaction patterns suggested by classical BA. BA-T is organized around three functional roles that implement this information flow: (1) cross-view correspondence estimation and latent residual computation, (2) camera update, and (3) geometry update. This BA-inspired architecture realizes the update flow through structured token interactions that directly predict parameter updates. Thanks to the structured updates, BA-T also outperforms naive iterative cross-attention stacks, as shown in section 4.2.

Formally, let $c_{a \rightarrow b} \in \mathbb{R}^{1 \times D}$ denote the camera token for an image pair $(\mathbf{I}_a, \mathbf{I}_b)$, where D is the token dimension. The camera token encodes relative pose from view a to view b . Let $\mathbf{g}_a, \mathbf{g}_b \in \mathbb{R}^{N \times D}$ denote the local geometry tokens for images \mathbf{I}_a and \mathbf{I}_b , with N tokens per image. The initial camera token $c_{a \rightarrow b}^{(0)}$ is a learnable parameter shared across all pairs, while the initial geometry tokens $\mathbf{g}_a^{(0)}$ and $\mathbf{g}_b^{(0)}$ are obtained from image features extracted by an image encoder.

BA-T, denoted as \mathcal{F}_θ , takes the set of camera and geometry tokens as input, computes latent residuals in the implicit token space, and updates camera and geometry tokens accordingly. Specifically, given the token set $\mathcal{T}^{(k)}$ from iteration k , $\mathcal{F}_\theta(\cdot)$ produces updated tokens,

$$\mathcal{T}^{(k)} = \left\{ c_{a \rightarrow b}^{(k)}, \mathbf{g}_a^{(k)}, \mathbf{g}_b^{(k)} \right\}, \quad \Delta \mathcal{T}^{(k)} = \mathcal{F}_\theta \left(\mathcal{T}^{(k)} \right), \quad \mathcal{T}^{(k+1)} = \mathcal{T}^{(k)} + \Delta \mathcal{T}^{(k)}. \quad (4)$$

This update process can be applied iteratively for a variable number of steps $k = 0, \dots, K$, where K is not fixed and may differ between training and inference. Through repeated refinement, BA-T progressively enforces global geometric consistency across views, following the same broad refinement spirit as bundle adjustment while remaining a learned latent model.



Figure 3: **Token-level correspondence response.** Given a local geometry token from one view, its attention scores highlight responses in the other view. Correct responses are observed for both ambiguous (left, middle) and distinctive (right) regions.

3.3 Implementation of General Functions in BA-T

Inspired by the general form of BA, we design the following components to support iterative refinement and information exchange between camera and geometry tokens: a camera-conditioned geometry alignment function $\pi_c^{a \rightarrow b}$, a property function f , and a residual function r . Additionally, given a geometry token g_a^p in view a , we must identify its corresponding geometry token g_b^q in view b .

Camera-Conditioned Geometry Transform. Since the geometry tokens of the two views are defined in their respective local frames, they are not directly comparable. We first focus on how to inject the camera token $c_{a \rightarrow b}$ into the geometry token g_a^p so that they can be compared consistently in a shared space. Since the local coordinates are linked via the relative transformation (which is encoded in the camera token), it is natural to aggregate information from the camera token $c_{a \rightarrow b}$ into the geometry token g_a^p of view a . Inspired by the conditioning mechanism in DiT [25], we implement this transformation using a condition block with an adaLN layer, which conditions the local geometry token g_a^p on the camera token $c_{a \rightarrow b}$: $\pi_c^{a \rightarrow b}(g_a^p) := \text{Condition}(g_a^p, c_{a \rightarrow b})$.

Token-level Correspondence Matching. Once the transformed geometry token is obtained, we match it with the corresponding geometry token g_b^q in view b to compute the residual. Since each token represents a local image patch, the projected region in the other view may not align exactly with a single token as in pixel-level matching, but can instead fall between tokens or span multiple tokens. Therefore, a flexible correspondence matching mechanism is required. We adopt an attention-inspired correspondence method. As shown in fig. 3, for a given transformed token $\pi_c^{a \rightarrow b}(g_a^p)$, a cross-attention layer queries the corresponding tokens in view b . We can then obtain the attention score α_p , measuring the relevance of the query token $\pi_c^{a \rightarrow b}(g_a^p)$ and every token in view b , and the corresponding token g_b^q is obtained as the attention-weighted sum of all geometry tokens in view b ,

$$\alpha_p = \text{AttnScore}(\pi_c^{a \rightarrow b}(g_a^p), \mathbf{g}_b), \quad g_b^q = \sum_{i < N} \alpha_p^i \cdot g_b^i. \quad (5)$$

This soft correspondence mechanism enables BA-T to model sub-token matches and occlusions that are difficult to capture with explicit classical BA.

Latent Property and Residual Function. For the property function $f(\cdot)$, we apply a linear projection to extract a suitable representation from each geometry token:

$$f(\pi_c^{a \rightarrow b}(g_a^p)) = \text{proj}(\pi_c^{a \rightarrow b}(g_a^p)), \quad f(g_b^q) = \text{proj}(g_b^q). \quad (6)$$

The function $r(\cdot, \cdot)$ that calculates residual in latent space is implemented as an MLP applied to the difference between the properties of the two tokens:

$$r_{a \rightarrow b}(f(g_b^q), f(\pi_c^{a \rightarrow b}(g_a^p))) = \text{MLP}(f(g_b^q) - f(\pi_c^{a \rightarrow b}(g_a^p))). \quad (7)$$

The resulting latent residual token encodes the discrepancy (fig. 4) between the geometry in view a (expressed in b 's space) and its corresponding region in view b , serving as a learned analogue of the classical residual (e.g., reprojection error).

Relative Camera Information Update Inspired by the information propagation pattern of classical BA in eq. (3), we update the camera token \mathbf{t}_c first at each iteration in BA-T. In practice, the camera update $\Delta c_{a \rightarrow b}$ is predicted from the current camera estimate $c_{a \rightarrow b}$ and the residual tokens $\mathbf{r}_{a \rightarrow b}$, which already carry the geometry information needed for the next refinement step. Thus, we update the camera token by attending from a single camera token to multiple residual-related tokens. Specifically, we employ a one-to-many cross-attention mechanism, where the camera token serves as

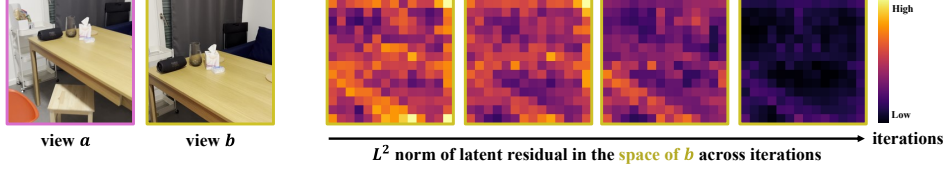


Figure 4: **Visualization of latent residuals.** Residuals are computed in the latent space of view b . Their magnitude decreases across refinement iterations, indicating increasingly accurate estimates.

the query and the residual tokens act as the context to be aggregated,

$$\Delta c_{a \rightarrow b}^{(k)} = \text{CrossAttn} \left(c_{a \rightarrow b}^{(k)}, \mathbf{r}_{a \rightarrow b}^{(k)} \right), \quad (8)$$

where $\text{CrossAttn}(\cdot, \cdot)$ denotes a cross-attention operator that aggregates information from multiple residual tokens conditioned on the current camera token. This one-to-many attention-based update implicitly captures the information flow of the camera update in Schur complement in classical BA.

Local Geometry Update After obtaining the camera update $\Delta c_{a \rightarrow b}$, we proceed to update the local geometries \mathbf{g}_a and \mathbf{g}_b . As the residual information $\mathbf{r}_{a \rightarrow b}$ has already been aggregated into the camera update $\Delta c_{a \rightarrow b}$, the geometry update depends on the current estimates of local geometry \mathbf{g}_a and \mathbf{g}_b , and the updated camera parameters $c_{a \rightarrow b}^{(k+1)} = c_{a \rightarrow b}^{(k)} + \Delta c_{a \rightarrow b}^{(k)}$.

To effectively exploit cross-view geometric consistency, we update the local geometry using cross-attention between the two views. Specifically, when updating the geometry of one view, we condition on both its own current geometry and the camera-conditioned geometry of the other view, so that both geometry are aligned in the same space,

$$\Delta \mathbf{g}_a^{(k)} = \text{CrossAttn} \left(\mathbf{g}_a^{(k)}, \pi_{c^{(k+1)}}^{b \rightarrow a} \left(\mathbf{g}_b^{(k)} \right) \right), \quad \Delta \mathbf{g}_b^{(k)} = \text{CrossAttn} \left(\mathbf{g}_b^{(k)}, \pi_{c^{(k+1)}}^{a \rightarrow b} \left(\mathbf{g}_a^{(k)} \right) \right). \quad (9)$$

This symmetric cross-view update encourages consistent geometric refinement across views and follows the same information propagation pattern as the geometry update step in classical BA, where local structure is refined conditioned on the updated camera parameters.

Together, these camera and geometry update steps form a complete iterative refinement procedure in BA-T, in which local geometry and relative camera parameters are progressively refined through repeated application of a single refinement layer.

3.4 Implementation and Training

We instantiate BA-T in a two-view reconstruction model that regresses local point maps and relative camera poses for an image pair, using a ViT [11] encoder to capture per-image features and decoding the implicit token from iterative BA-T into per-view point maps and relative camera pose using regression heads (more details are provided in Appendix section A).

Loss functions. The supervision signals include point-level geometry, relative pose, and cross-view consistency constraints, following standard choices in prior works [42, 10, 49]. The overall training objective is defined as

$$L = \lambda_{\text{pmap}} L_{\text{pmap}} + \lambda_{\text{pose}} L_{\text{pose}} + \lambda_{\text{gc}} L_{\text{gc}}, \quad (10)$$

where L_{pmap} supervises the predicted local point maps, L_{pose} penalizes errors in relative rotation and translation with an additional cycle-consistency constraint, and L_{gc} enforces geometric consistency between point maps across views under the predicted relative transformation. The weighting factors λ_{pmap} , λ_{pose} , and λ_{gc} balance the three terms.

Iterative Supervision. Since BA-T refines camera and geometry tokens over multiple iterations using the same Transformer layer, we apply supervision at the output of each iteration. Let $L^{(k)}$ denote the loss at iteration k , and let K be the total number of iterations. To encourage progressive refinement, later iterations are given higher weights, while earlier iterations contribute less. This design ensures the network learns to gradually refine predictions rather than only focusing on the final output.

$$L_{\text{total}} = \sum_{k=1}^K \alpha_\lambda^{K-k} L^{(k)}, \quad (0 < \alpha_\lambda < 1) \quad (11)$$

Table 1: **Relative pose and geometry evaluation on 7Scenes [30] and BundleFusion [8].** BA-T ($K = 4$) achieves best pose and competitive geometry performance among two-view methods, while maintaining a significantly smaller decoder size.

Method	7Scenes								BundleFusion						Decoder Param Size #↓
	Pose AUC				Geometry				Pose AUC			Geometry			
	@5° ↑	@10° ↑	@20° ↑	Chamf. ↓	Acc. ↓	Comp. ↓	$\delta_{1.25}$ ↑	@5° ↑	@10° ↑	@20° ↑	Chamf. ↓	Acc. ↓	Comp. ↓	$\delta_{1.25}$ ↑	
<i>Trained with Multi-view Data</i>															
VGGT [39]	0.19	0.39	0.60	0.10	0.10	0.07	0.97	0.18	0.36	0.56	0.06	0.07	0.04	0.99	605M
MA [17]	0.09	0.23	0.44	0.10	0.12	0.07	0.98	0.03	0.11	0.27	0.15	0.19	0.09	0.98	171M
DA3 [19]	0.22	0.43	0.64	0.08	0.09	0.06	0.98	0.20	0.37	0.57	0.06	0.07	0.04	0.99	765M
<i>Trained with Two-view Data</i>															
DUST3R [42]	0.09	0.22	0.42	0.13	0.13	0.12	0.81	0.16	0.33	0.52	0.25	0.26	0.22	0.58	227M
MASt3R [18]	0.15	0.32	0.52	0.16	0.16	0.11	0.79	0.16	0.32	0.50	0.24	0.26	0.22	0.58	227M
ViSTA [49]	0.13	0.33	0.56	0.10	0.10	0.10	0.98	0.15	0.31	0.51	0.06	0.06	0.05	0.99	113M
ViSTA [†] [49]	0.01	0.06	0.17	0.15	0.12	0.15	0.94	0.02	0.07	0.17	0.09	0.09	0.09	0.98	38M
BA-T	0.16	0.37	0.59	0.11	0.10	0.11	0.98	0.16	0.34	0.54	0.07	0.07	0.06	0.99	38M

4 Experiments

We present the evaluation of BA-T in three parts. First, we compare it with recent feed-forward 3D reconstruction models with deep stacked decoders to assess pose estimation and geometry reconstruction results. Next, we analyze the performance of iterative refinements. Finally, we ablate the components of BA-T and discuss its potentials and limitations. Best results are highlighted as **first** and **second**.

4.1 Evaluation of Pose Estimation and 3D Reconstruction

In table 1, BA-T (with $K = 4$ iterations for inference) is compared with recent feedforward 3D reconstruction models trained with multi-view data [39, 17, 19] and with two-view data [42, 18, 49]. Since these models employ much larger architectures than BA-T, we train an additional variant of ViSTA [49] with a decoder size comparable to BA-T, denoted as ViSTA[†], to enable a fair comparison.

Metrics and Datasets. We evaluate both pose estimation and geometry reconstruction. For relative pose, we report $\text{AUC}@5^\circ/10^\circ/20^\circ$, computed as the area under the pose accuracy curve with thresholds $5^\circ/10^\circ/20^\circ$, where the pose error is the maximum of rotation and translation angular errors. For geometry, we report Chamfer distance, accuracy, completeness, and depth threshold accuracy $\delta_{1.25}$, defined as the percentage of pixels satisfying $\max(y_{\text{pred}}/y_{\text{gt}}, y_{\text{gt}}/y_{\text{pred}}) < 1.25$, capturing local geometric quality. Evaluation uses 3,600 and 1,109 co-visible image pairs from real world datasets 7Scenes [30] and BundleFusion [8], which provide ground-truth camera poses and 3D geometry.

Results. As shown in table 1, BA-T achieves the best overall pose estimation among two-view models. It even delivers competitive results compared to models trained on multi-view data, despite having a significantly lighter structure (5% of their size). For geometry, BA-T performs on par with substantially larger models. Compared to a model with similar decoder size, *i.e.*, ViSTA[†] [49], BA-T consistently outperforms in both pose and geometry metrics, demonstrating the effectiveness of structured iterative refinement. Notably, it achieves this with a compact reusable layer (38M parameters), much smaller than prior methods (113M–765M), balancing accuracy and efficiency (running speed and memory footprint are reported in the Appendix table 5).

4.2 Performance under Iterative Refinements

Setup and Metrics. To evaluate the effectiveness of iterative refinement in BA-T, we analyze performance across multiple update steps. For comparison, we also train a variant of ViSTA[†] [49] using the same training settings as BA-T. This variant, denoted as ViSTA[†] *w/ iterative training*, employs iterative training in the same manner as BA-T. The only difference is that this baseline performs iteration with a conventional cross-view attention stacked decoder design, whereas BA-T adopts a BA-inspired structured update mechanism. We report rotation (in degrees) and translation (in meters) AUCs, along with geometry metrics: relative depth error (Rel.) and depth threshold accuracies $\delta_{1.05}$, $\delta_{1.25}$, to evaluate local geometry quality; 3D correspondence error (Corr.), which is the Euclidean distance between corresponding 3D points from two images, and is used to assess the consistency of the local 3D reconstructions across the two views, with ground-truth correspondences obtained from GT depths and camera poses.

Table 2: (left) **Performance comparison on 7Scenes [30] across iterative refinement steps.** Increasing the number of refinement iterations consistently improves pose and geometry accuracy. ViSTA[†] w/ iterative training performs iterative update by conventional stacked decoder with comparable size. BA-T outperforms it at all iterations, showing the effectiveness of the proposed structural design.

Figure 5: (right) **Iterative refinement behavior.** BA-T (green curve) consistently outperforms ViSTA[†] w/ iterative training (red curve) and converges within 3 ~ 4 refinement steps.

Method	Iter	Rot. AUC (deg)			Trans. AUC (m)			Geometry			Decoder Size #	
		@5°↑	@10°↑	@20°↑	@0.05↑	@0.10↑	@0.20↑	Corr.↓	Rel.↓	$\delta_{1.05}$ ↑		$\delta_{1.25}$ ↑
ViSTA [†]	/	0.426	0.662	0.823	0.104	0.272	0.510	0.052	0.079	0.380	0.940	38M
ViSTA [†] w/ iterative training	1	0.442	0.676	0.830	0.101	0.270	0.505	0.062	0.061	0.497	0.967	38M
	2	0.472	0.699	0.844	0.133	0.322	0.555	0.048	0.060	0.513	0.968	
	3	0.485	0.708	0.848	0.146	0.341	0.575	0.045	0.060	0.515	0.968	
	4	0.491	0.712	0.851	0.151	0.346	0.580	0.045	0.060	0.516	0.968	
BA-T	1	0.650	0.819	0.908	0.322	0.555	0.749	0.046	0.051	0.569	0.972	38M
	2	0.671	0.830	0.914	0.401	0.624	0.794	0.032	0.050	0.585	0.975	
	3	0.679	0.834	0.916	0.421	0.642	0.805	0.028	0.049	0.594	0.976	
	4	0.683	0.836	0.917	0.422	0.643	0.805	0.026	0.048	0.601	0.976	

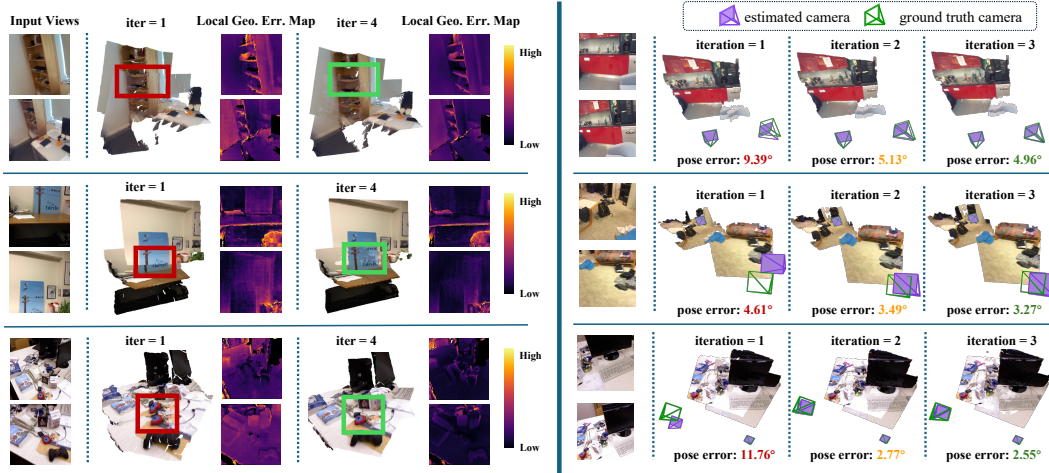
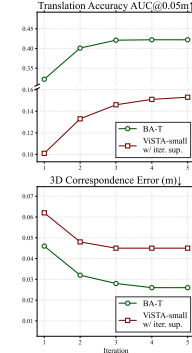


Figure 6: (left) **Qualitative reconstruction results.** We visualize reconstructed geometry and 3D points (in local frame) error maps at iteration 1 and iteration 4. **Red boxes** highlight noticeable misalignments in the 1st iteration, which are corrected in the 4th iteration, as indicated by **green boxes**. This demonstrates the effectiveness of the iterative refinement in BA-T for improving local geometric consistency. (right) **Pose estimation visualization.** Estimated relative poses across different refinement iterations are shown. BA-T progressively refines the pose estimates over iterations and remains robust even in low-visibility cases (second row).

Quantitative Results. As shown in table 2, iterative refinement in BA-T steadily improves both pose and geometry. Both pose and geometry metrics get better across iterations, reflecting consistent gains in reconstruction. Most improvements occur within the first 3–4 iterations (fig. 5), after which performance converges. For comparison, ViSTA[†] [49] reduces 3D correspondence error by only 27%, whereas BA-T achieves 44%, showing that our BA-inspired design more effectively enforces reconstruction consistency. Results demonstrate that structured iterative updates in BA-T efficiently refine camera poses and 3D geometry, enabling high-accuracy reconstruction with a compact layer.

Qualitative Results. In fig. 6 (left), we show reconstruction results after 1 and 4 iterations, along with 3D points error maps, for scenes from 7Scenes [30], BundleFusion [8], and TUM-RGBD [32]. After the first iteration, local geometry roughly captures the scene, but cross-view alignment is still inaccurate, producing misaligned planes and edges. Subsequent iterations progressively correct these discrepancies, yielding better-aligned structures, sharper details, demonstrating improved consistency through structured iterative updates. In fig. 6 (right), it shows geometry and relative camera poses from iteration 1 to 3. Estimated poses become increasingly accurate with each iteration. Notably, in cases with very limited visual overlap (e.g., only a small co-visible region), BA-T still gradually refines camera poses, demonstrating its robustness under challenging low-overlap conditions.

Table 3: **Ablation study of BA-T.** Removing any component degrades pose and geometry performance, emphasizing each module’s contribution. The full BA-T model achieves the best results.

Setting	Rot. AUC (deg)			Trans. AUC (m)			Geometry Reconstruction			
	@5° ↑	@10° ↑	@20° ↑	@0.05↑	@0.10↑	@0.20↑	Corr.↓	Rel.↓	$\delta_{1.05}$ ↑	$\delta_{1.25}$ ↑
w/o Iterative Supervision	0.667	0.827	0.912	0.404	0.625	0.793	0.036	0.049	0.620	0.974
w/o Correspondence Matching	0.677	0.833	0.916	0.412	0.635	0.802	0.026	0.048	0.591	0.976
w/o Geometry Transform	0.665	0.827	0.912	0.385	0.613	0.787	0.027	0.050	0.599	0.974
Ours (Full BA-T)	0.683	0.836	0.917	0.422	0.643	0.805	0.026	0.048	<u>0.601</u>	0.976

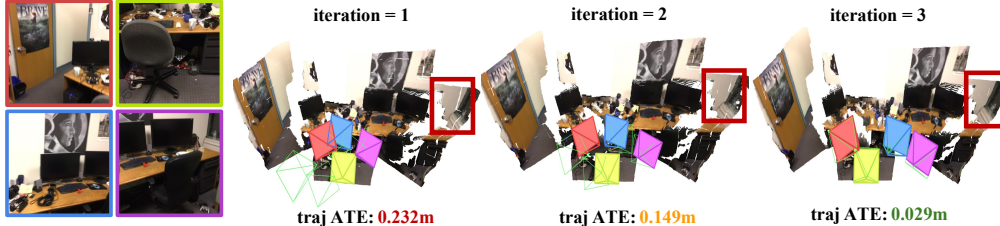


Figure 7: **Multiview reconstruction results.** Estimated poses and reconstructed scenes are visualized across iterations for a 4-view input setup, demonstrating BA-T’s ability to handle multi-view settings. The green frustums indicate GT camera poses. The red boxes and decreasing trajectory ATE (0.232m → 0.029m) highlights the effectiveness of iterative refinements.

4.3 Ablation: Effectiveness of Components in BA-T

In table 3, we ablate components of BA-T. Using all proposed modules yields the best overall performance on both camera pose and 3D reconstruction metrics. Iterative supervision improves both pose and cross-view consistency. Removing it reduces rotation and translation accuracy, and increases 3D correspondence error, indicating that it improves convergence. Correspondence tokens mainly enhance relative pose. Without them, local geometry remains similar, but rotation and translation AUC drop, suggesting these tokens facilitate cross-view pose alignment more than per-view geometry. Geometry transform is critical for refinement. Removing it forces the network to operate directly in the two different local coordinate spaces of the input views, making refinement more challenging, degrading both pose and geometry metrics, showing that alignment across views is essential for effective scene token updates. Overall, the full BA-T achieves the strongest results, highlighting the importance of structured token interaction for accurate pose estimation and geometry.

4.4 Extension: BA-T for Multiview Reconstruction

Thanks to the BA-inspired design, all cross-view interactions in BA-T are performed in view’s local space, making it possible to directly extend to multi-view inputs *without* architectural changes. The most straightforward way for multiview extension is to allow each query view to attend to all other views, producing per-view pointmaps (details in Appendix). Visualization of a multiview example is shown in fig. 7. More importantly, the model refines all related views together, allowing information from one view to immediately help improve the others and strengthen overall consistency. This makes BA-T a natural fit for multi-view reconstruction and allows it to scale beyond the two-view setting.

While our design is not inherently limited to two views, the current implementation and training mainly focus on two-view reconstruction, broader multi-view configurations remain unexplored. Future work includes integrating BA-T into multi-view reconstruction frameworks [39, 19] to replace cross-view attention decoders and leverage large-scale data, potentially improving global consistency and reconstruction accuracy.

5 Conclusion

We propose BA-T, a Bundle-Adjustment-inspired iterative Transformer that jointly refines camera poses and 3D geometry via an implicit, structured, learnable BA-inspired layer. Unlike conventional feed-forward decoders that predict in a single pass, BA-T enables coordinated, progressive refinement within a compact architecture. Experiments show it consistently improves pose and geometry estimates across iterations, achieves stronger consistency than standard stacked-attention decoders, and delivers high-accuracy pose estimation and 3D reconstruction efficiently.

References

- [1] Agarwal, S., Snavely, N., Seitz, S.M., Szeliski, R.: Bundle adjustment in the large. In: ECCV. pp. 29–42. Springer (2010)
- [2] Alismail, H., Browning, B., Lucey, S.: Photometric bundle adjustment for vision-based slam. In: ACCV. pp. 324–341. Springer (2016)
- [3] Avetisyan, A., Xie, C., Howard-Jenkins, H., Yang, T.Y., Aroudj, S., Patra, S., Zhang, F., Frost, D., Holland, L., Orme, C., et al.: Scenescrypt: Reconstructing scenes with an autoregressive structured language model. In: ECCV. pp. 247–263. Springer (2024)
- [4] Baruch, G., Chen, Z., Dehghan, A., Dimry, T., Feigin, Y., Fu, P., Gebauer, T., Joffe, B., Kurz, D., Schwartz, A., Shulman, E.: ARKitScenes - a diverse real-world dataset for 3D indoor scene understanding using mobile RGB-D data. In: NeurIPS (2021)
- [5] Cabon, Y., Stoffl, L., Antsfeld, L., Csurka, G., Chidlovskii, B., Revaud, J., Leroy, V.: MUsT3R: Multi-view network for stereo 3D reconstruction. In: CVPR. pp. 1050–1060 (2025)
- [6] Carlone, L., Kim, A., Barfoot, T., Cremers, D., Dellaert, F. (eds.): SLAM Handbook. From Localization and Mapping to Spatial Intelligence. Cambridge University Press (2026)
- [7] Dai, A., Chang, A.X., Savva, M., Halber, M., Funkhouser, T., Nießner, M.: ScanNet: Richly-annotated 3D reconstructions of indoor scenes. In: CVPR (2017)
- [8] Dai, A., Nießner, M., Zollöfer, M., Izadi, S., Theobalt, C.: BundleFusion: Real-time globally consistent 3D reconstruction using on-the-fly surface re-integration. ACM TOG (2017)
- [9] Davison, A.J., Reid, I.D., Molton, N.D., Stasse, O.: MonoSLAM: Real-time single camera SLAM. IEEE TPAMI **29**(6), 1052–1067 (2007)
- [10] Dong, S., Wang, S., Liu, S., Cai, L., Fan, Q., Kannala, J., Yang, Y.: Reloc3r: Large-scale training of relative camera pose regression for generalizable, fast, and accurate visual localization. In: CVPR. pp. 16739–16752 (2025)
- [11] Dosovitskiy, A., Beyer, L., Kolesnikov, A., Weissenborn, D., Zhai, X., Unterthiner, T., Dehghani, M., Minderer, M., Heigold, G., Gelly, S., et al.: An image is worth 16x16 words: Transformers for image recognition at scale. In: ICLR (2021)
- [12] Engel, J., Koltun, V., Cremers, D.: Direct sparse odometry. IEEE TPAMI **40**(3), 611–625 (2017)
- [13] Engel, J., Schöps, T., Cremers, D.: LSD-SLAM: Large-scale direct monocular SLAM. In: ECCV. pp. 834–849. Springer (2014)
- [14] Gao, X., Wang, R., Demmel, N., Cremers, D.: LDSO: Direct sparse odometry with loop closure. In: 2018 IEEE/RSJ International Conference on Intelligent Robots and Systems (IROS). pp. 2198–2204. IEEE (2018)
- [15] Hagemann, A., Knorr, M., Stiller, C.: Deep geometry-aware camera self-calibration from video. In: ICCV. pp. 3438–3448 (October 2023)
- [16] Hartley, R., Zisserman, A.: Multiple view geometry in computer vision. Cambridge university press (2003)
- [17] Keetha, N., Müller, N., Schönberger, J., Porzi, L., Zhang, Y., Fischer, T., Knapitsch, A., Zauss, D., Weber, E., Antunes, N., Luiten, J., Lopez-Antequera, M., Bulò, S.R., Richardt, C., Ramanan, D., Scherer, S., Kotschieder, P.: MapAnything: Universal feed-forward metric 3D reconstruction. In: International Conference on 3D Vision (3DV). IEEE (2026)
- [18] Leroy, V., Cabon, Y., Revaud, J.: Grounding image matching in 3D with MAsT3R. In: ECCV. pp. 71–91. Springer (2024)
- [19] Lin, H., Chen, S., Liew, J.H., Chen, D.Y., Li, Z., Shi, G., Feng, J., Kang, B.: Depth Anything 3: Recovering the visual space from any views. arXiv preprint arXiv:2511.10647 (2025)
- [20] Liu, S., Gao, Y., Zhang, T., Pautrat, R., Schönberger, J.L., Larsson, V., Pollefeys, M.: Robust incremental structure-from-motion with hybrid features. In: ECCV. pp. 249–269. Springer (2024)
- [21] Loshchilov, I., Hutter, F.: Decoupled weight decay regularization. arXiv preprint arXiv:1711.05101 (2017)

- [22] Mur-Artal, R., Montiel, J.M.M., Tardos, J.D.: ORB-SLAM: A versatile and accurate monocular SLAM system. *IEEE transactions on robotics* **31**(5), 1147–1163 (2015)
- [23] Nocedal, J., Wright, S.J.: *Numerical optimization*. Springer (2006)
- [24] Pan, L., Baráth, D., Pollefeys, M., Schönberger, J.L.: Global structure-from-motion revisited. In: *ECCV*. pp. 58–77. Springer (2024)
- [25] Peebles, W., Xie, S.: Scalable diffusion models with transformers. In: *ICCV*. pp. 4195–4205 (2023)
- [26] Qian, S., Zhang, G., Wu, S., Cremers, D.: Flow4R: Unifying 4d reconstruction and tracking with scene flow. *arXiv preprint arXiv:2602.14021* (2026)
- [27] Reizenstein, J., Shapovalov, R., Henzler, P., Sbordone, L., Labatut, P., Novotny, D.: Common objects in 3D: Large-scale learning and evaluation of real-life 3D category reconstruction. In: *ICCV* (2021)
- [28] Sandström, E., Zhang, G., Tateno, K., Oechsle, M., Niemeyer, M., Zhang, Y., Patel, M., Van Gool, L., Oswald, M., Tombari, F.: Splat-SLAM: Globally optimized rgb-only SLAM with 3D gaussians. In: *CVPRW* (2025)
- [29] Schonberger, J.L., Frahm, J.M.: Structure-from-motion revisited. In: *CVPR*. pp. 4104–4113 (2016)
- [30] Shotton, J., Glocker, B., Zach, C., Izadi, S., Criminisi, A., Fitzgibbon, A.: Scene coordinate regression forests for camera relocalization in RGB-D images. In: *CVPR*. pp. 2930–2937 (2013)
- [31] Straub, J., Whelan, T., Ma, L., Chen, Y., Wijmans, E., Green, S., Engel, J.J., Mur-Artal, R., Ren, C., Verma, S., Clarkson, A., Yan, M., Budge, B., Yan, Y., Pan, X., Yon, J., Zou, Y., Leon, K., Carter, N., Briales, J., Gillingham, T., Mueggler, E., Pesqueira, L., Savva, M., Batra, D., Strasdat, H.M., Nardi, R.D., Goesele, M., Lovegrove, S., Newcombe, R.: The Replica dataset: A digital replica of indoor spaces. *arXiv preprint arXiv:1906.05797* (2019)
- [32] Sturm, J., Engelhard, N., Endres, F., Burgard, W., Cremers, D.: A benchmark for the evaluation of RGB-D SLAM systems. In: *IROS* (Oct 2012)
- [33] Tang, C., Tan, P.: BA-Net: Dense bundle adjustment network. In: *ICLR* (2019)
- [34] Teed, Z., Deng, J.: RAFT: Recurrent all-pairs field transforms for optical flow. In: *ECCV*. pp. 402–419. Springer (2020)
- [35] Teed, Z., Deng, J.: DROID-SLAM: Deep visual SLAM for monocular, stereo, and RGB-D cameras. *NeurIPS* **34**, 16558–16569 (2021)
- [36] Teed, Z., Lipson, L., Deng, J.: Deep patch visual odometry. *NeurIPS* **36**, 39033–39051 (2023)
- [37] Triggs, B., McLauchlan, P.F., Hartley, R.I., Fitzgibbon, A.W.: Bundle adjustment—a modern synthesis. In: *International workshop on vision algorithms*. pp. 298–372. Springer (1999)
- [38] Wang, H., Agapito, L.: 3D reconstruction with spatial memory. In: *3DV* (2025)
- [39] Wang, J., Chen, M., Karaev, N., Vedaldi, A., Ruppert, C., Novotny, D.: VGGT: Visual geometry grounded transformer. In: *CVPR* (2025)
- [40] Wang, J., Karaev, N., Ruppert, C., Novotny, D.: VGGsFM: Visual geometry grounded deep structure from motion. In: *CVPR*. pp. 21686–21697 (2024)
- [41] Wang, Q., Zhang, Y., Holynski, A., Efros, A.A., Kanazawa, A.: Continuous 3D perception model with persistent state. In: *CVPR*. pp. 10510–10522 (2025)
- [42] Wang, S., Leroy, V., Cabon, Y., Chidlovskii, B., Revaud, J.: DUST3R: Geometric 3D vision made easy. In: *CVPR*. pp. 20697–20709 (2024)
- [43] Wang, Y., Zhou, J., Zhu, H., Chang, W., Zhou, Y., Li, Z., Chen, J., Pang, J., Shen, C., He, T.: π^3 : Scalable permutation-equivariant visual geometry learning (2025)
- [44] Xu, H., Barath, D., Geiger, A., Pollefeys, M.: Resplat: Learning recurrent gaussian splats. *arXiv preprint arXiv:2510.08575* (2025)
- [45] Yang, N., Stumberg, L.v., Wang, R., Cremers, D.: D3VO: Deep depth, deep pose and deep uncertainty for monocular visual odometry. In: *CVPR*. pp. 1281–1292 (2020)
- [46] Yang, N., Wang, R., Stuckler, J., Cremers, D.: Deep virtual stereo odometry: Leveraging deep depth prediction for monocular direct sparse odometry. In: *ECCV*. pp. 817–833 (2018)

- [47] Yeshwanth, C., Liu, Y.C., Nießner, M., Dai, A.: ScanNet++: A high-fidelity dataset of 3D indoor scenes. In: ICCV (2023)
- [48] Yuan, Y., Chen, Z., Li, K., Wang, W., Zhao, H.: SLAM-Former: Putting SLAM into one transformer. arXiv preprint arXiv:2509.16909 (2025)
- [49] Zhang, G., Qian, S., Wang, X., Cremers, D.: ViSTA-SLAM: Visual SLAM with symmetric two-view association. arXiv preprint arXiv:2509.01584 (2025)
- [50] Zhang, G., Sandström, E., Zhang, Y., Patel, M., Van Gool, L., Oswald, M.R.: GIORIE-SLAM: Globally optimized RGB-only implicit encoding point cloud SLAM. arXiv preprint arXiv:2403.19549 (2024)
- [51] Zhang, W., Cheng, Q., Skuddis, D., Zeller, N., Cremers, D., Haala, N.: HI-SLAM2: Geometry-aware gaussian SLAM for fast monocular scene reconstruction. arXiv preprint arXiv:2411.17982 (2024)
- [52] Zhang, W., Sun, T., Wang, S., Cheng, Q., Haala, N.: HI-SLAM: Monocular real-time dense mapping with hybrid implicit fields. IEEE Robotics and Automation Letters **9**(2), 1548–1555 (2023)

BA-T: An Iterative Transformer for Two-View Bundle Adjustment

Appendix

A Architecture and Training Details

Architecture Details. In BA-T, tokens have dimension $D = 768$. In the Space Transform module, geometry tokens are transformed using an AdaLN-style conditional block [25], where each token is normalized and modulated with shift and scale vectors predicted from the camera token (also 768-D). Token-level Correspondence Matching uses 8 attention heads, enabling tokens from different views to interact and establish geometric correspondences. The Latent Property and Residual Function applies linear projections to matched tokens, followed by a 2-layer MLP with expansion ratio 4 to produce normalized residuals that inform the camera update. The camera token is updated through cross-attention (12 heads) and a 2-layer feed-forward MLP with expansion ratio 4. Local geometry tokens are refined via cross-view attention (12 heads, 2-layer MLP with expansion ratio 4) and three intra-view self-attention layers (each with 12 heads and a 2-layer MLP with expansion ratio 4) to improve per-view feature consistency. Training uses $K = 5$ iterations for iterative supervision.

Training Details. We initialize the encoder with a pretrained ViT [49], while BA-T and the regression heads are randomly initialized. All components are trained jointly. Following the setting of prior work [49], BA-T is trained on ScanNet [7], ScanNet++ [47], ARKitScenes [4], CO3D [27], ASE [3], and Replica [31], for 2 days on 8 NVIDIA H100 GPUs. Training uses AdamW [21] with a learning rate of 1.5×10^{-4} , weight decay 0.01, and $\alpha_\lambda = 0.8$, $K = 5$.

B Bidirectional Camera Representation

In BA-T, each two-view pair is represented by a single camera token that encodes the relative transformation. However, the local geometry update requires both directions of the relative transformation, and the camera-conditioned operator $\pi_{c_{b \rightarrow a}^{(k+1)}}^{b \rightarrow a}(\cdot)$ still depends on the camera parameters $c_{b \rightarrow a}^{(k+1)}$. To obtain the opposite direction of the transformation, we recover $c_{b \rightarrow a}$ by applying a lightweight MLP to $c_{a \rightarrow b}$. This MLP learns the inverse transformation in latent space, which avoids redundant camera tokens while preserving bidirectional geometric consistency.

C Solver-based BA Comparison

We further compare BA-T with Droid-SLAM, which relies on classical bundle adjustment (BA) using reprojection error as the residual and Gauss–Newton as the optimizer. For a fair comparison, both methods are initialized with the same local geometry and camera poses (taken from iteration 0 of BA-T). Since Droid-SLAM requires camera calibration, we additionally provide the ground-truth intrinsic matrix. Quantitative and qualitative results are reported in table 4 and fig. 8, respectively. The results show that classical BA underperforms compared to BA-T, particularly in geometry reconstruction. This is largely due to the highly non-convex optimization objective, which is difficult to solve reliably under limited co-visibility constraints (e.g., few-view settings). In contrast, BA-T benefits from expressive latent representations and learned priors from training data, leading to improved robustness and accuracy. Moreover, BA-T is substantially more efficient, achieving approximately $5 \times$ faster inference while reducing memory consumption by about 45%.

Table 4: **Quantitative comparison of two-view inputs on 7Scenes [30].**

Method	Rot AUC @5°	Trans AUC @0.05m	Rel. $\delta < 1.25$	Time (ms)	Peak Mem (GB)
Droid-SLAM [35]	0.53	0.08	1.19	160.93	2.43
BA-T	0.68	0.42	0.20	30.92	1.35

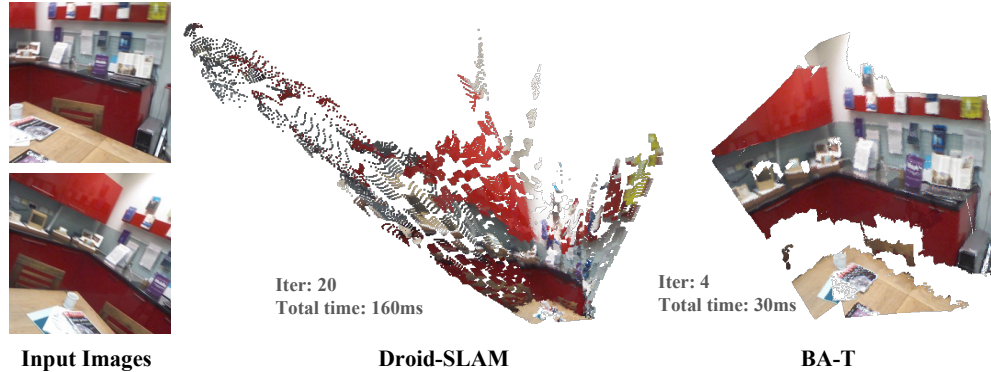


Figure 8: **Reconstruction comparison.** Both methods are initialized from BA-T (iter = 0). Droid-SLAM uses ground-truth intrinsics, whereas BA-T does not. BA-T achieves stronger performance with fewer iterations and faster runtime, benefiting from its more expressive latent space.

D Running Time and Peak Memory

We evaluate BA-T against several multiview [39, 19, 17] and two-view [35, 18, 42, 49] methods under the two-view setting, measuring decoder size, peak GPU memory, and inference time on the same input images with the same resolution. As shown in table 5, BA-T achieves the most compact architecture with only 38M parameters, substantially smaller than all prior methods. It also requires the lowest peak memory (1.32 GB) and delivers faster inference, demonstrating a significant improvement in computational efficiency while maintaining competitive accuracy. These results highlight the effectiveness of BA-T’s compact and iterative design.

Table 5: **Model size and efficiency comparison under two-view inputs.** Decoder size is reported in millions of parameters (M), peak GPU memory in GB, and running time in milliseconds (ms). BA-T achieves the most compact architecture and the highest computational efficiency among all compared methods.

	Droid [35]	VGGT [39]	DA3 [19]	MapAny [17]	MASt3R [18]	DUS _t 3R [42]	ViSTA [49]	BA-T ($k=1/2/3/4$)
Running time ↓ (ms)	160.93	128.71	78.14	41.13	93.25	66.47	37.96	21.40 / 24.65 / 28.32 / 30.92
Decoder size ↓ (M)	/	605	765	171	227	227	113	38
Peak GPU mem ↓ (GB)	2.43	4.93	6.52	3.23	2.72	2.02	1.76	1.32

E Discussion on Iteration and Refinement Behavior

E.1 Comparison with Unrolling and Recurrent Methods

Although BA-T is inspired by the iterative refinement spirit of bundle adjustment, it differs from prior unrolling and recurrent methods in both the representation it updates and the role played by each iteration. BA-Net [33], RAFT [34], ReSplat [44], and BA-T all share an iterative refinement flavor, but the differences are substantial. BA-Net unrolls BA-style updates on explicit geometric variables, RAFT iteratively refines dense correspondence fields for optical flow, and ReSplat recurrently updates latent representations for Gaussian-splat novel-view synthesis; in all three cases, the update target and problem setting differ a lot from ours. The ablation with ViSTA[†] using iterative training supports the same point: iterative training helps, but a large gap remains compared to BA-T, indicating that iteration alone is not enough. By contrast, BA-T performs the refinement entirely in latent space and is designed around the BA structural information propagation path, where camera and geometry tokens exchange information through a compact, reusable refinement layer. In other words, our method is not just iterative in the generic sense: it is specifically structured to propagate information between camera and geometry in a reconstruction setting, rather than unrolling an explicit solver or recurrently refining flow or rendering variables.

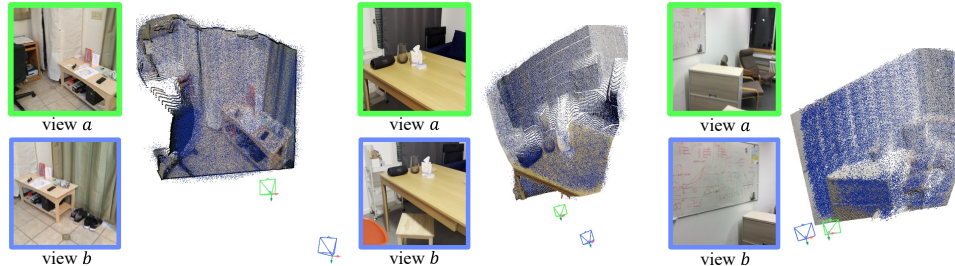


Figure 9: **Visualization of camera-conditioned geometry transformation.** Given two input views, a and b , we visualize the point map regressed from the geometry tokens g_a of view a as colored point clouds in the **coordinate frame of view a** . We also visualize the point map regressed from the transformed tokens $\pi_c^{a \rightarrow b}(g_a)$, which is obtained by conditioning g_a on the camera token $c_{a \rightarrow b}$, as blue point clouds in the **coordinate frame of view b** . The two point clouds align closely under the pose transformation encoded in the camera token, demonstrating that the Camera-Conditioned Geometry Transform component of BA-T operates as intended by transforming latent local geometry into the coordinate frames of other views.

E.2 Pose and Geometry Behavior in Experiments

In our experiments, pose estimation improves more consistently than geometry reconstruction, while the geometry gains are more limited. This behavior follows from the update design: the residual tokens directly influence the camera update, so pose benefits from a more immediate refinement signal. Geometry, in contrast, is updated after the camera has been refined, so its improvement is more indirect.

Another factor is that we reconstruct geometry on a per-view basis. The final scene geometry is therefore formed by combining the local geometry predictions with the estimated camera poses, rather than by optimizing a single global geometry representation at once. As a result, the local geometry outputs may not look dramatically different even when the pose estimates improve substantially.

This is why the quantitative gains are often clearer for pose than for geometry. The refinement process mainly strengthens the camera-geometry interaction, and the benefit to reconstruction is accumulated through the updated poses and the per-view local reconstructions.

E.3 Component-Level Behavior

In fig. 9, we also visualize the camera-conditioned geometry transform component by comparing the geometry regressed directly from the local geometry tokens with the geometry regressed from the camera-conditioned transformed tokens. The two geometry predictions roughly align under the provided camera transform, which shows that the transform behaves as designed.

Together with the correspondence and residual visualizations already shown in the main text, it provides component-level evidence that the learned modules follow the intended BA-inspired behavior. Although we do not explicitly train each component to exactly match its BA counterpart, the end-to-end training results show that the learned modules still roughly play the intended functional roles. This further supports the view that the BA-inspired structural design is valuable.

F Multiview Extension Details

To extend BA-T to the multi-view setting, we generalize the two-view formulation (algorithm 1) to operate on multiview inputs. Additionally, it requires a view graph $\mathcal{G}(\mathcal{V}, \mathcal{E})$ as input, where each node $i \in \mathcal{V}$ represents a view with geometry tokens g_i , and each edge $(i, j) \in \mathcal{E}$ is associated with a relative camera token $c_{i \rightarrow j}$. The overall architecture of BA-T remains unchanged; the same refinement layer is applied without any modification to the network structure. The only difference lies in how tokens interact according to the view graph connectivity, shown in algorithm 2.

For each edge (i, j) , residual tokens $r_{i \rightarrow j}$ are computed using the same procedure as in the two-view case: geometry tokens from view i are first transformed into view j using the camera token $c_{i \rightarrow j}$, latent correspondences are then obtained, and residuals are computed in latent space. Camera tokens

are subsequently updated independently for each edge using cross-attention between the camera token and its associated residual tokens.

The only difference from the two-view formulation arises in the local geometry update. Instead of performing cross-attention between a pair of views, each view attends to geometry tokens from all neighboring views in the graph, transformed into the same coordinate frame using the updated camera tokens. This effectively changes the interaction from a one-view-to-one-view cross-attention to a one-view-to-many-views cross-attention, allowing each view to aggregate multiview geometric constraints.

Importantly, this extension does not modify the network architecture: the same refinement layer and parameters are reused without introducing additional modules or increasing the model depth or width. The multiview capability therefore emerges purely from the changed token connectivity defined by the input view-graph.

Algorithm 1: Two-view BA-T

Input: $\mathbf{g}_a^{(k)}, \mathbf{g}_b^{(k)}, c_{a \rightarrow b}^{(k)}$
Output: $\mathbf{g}_a^{(k+1)}, \mathbf{g}_b^{(k+1)}, c_{a \rightarrow b}^{(k+1)}$
// Residual computation
 $\tilde{\mathbf{g}}_a^{(k)} \leftarrow \pi_{c_{a \rightarrow b}^{(k)}}(\mathbf{g}_a^{(k)})$
 $\tilde{\mathbf{g}}_b^{(k)} \leftarrow \text{LatentMatch}(\tilde{\mathbf{g}}_a^{(k)}, \mathbf{g}_b^{(k)})$
 $\mathbf{r}_{a \rightarrow b}^{(k)} \leftarrow \text{MLP}(f(\tilde{\mathbf{g}}_b^{(k)}) - f(\tilde{\mathbf{g}}_a^{(k)}))$
// Camera update
 $\Delta c_{a \rightarrow b}^{(k)} \leftarrow \text{CrossAttn}(c_{a \rightarrow b}^{(k)}, \mathbf{r}_{a \rightarrow b}^{(k)})$
 $c_{a \rightarrow b}^{(k+1)} \leftarrow c_{a \rightarrow b}^{(k)} + \Delta c_{a \rightarrow b}^{(k)}$
// Geometry update
 $\Delta \mathbf{g}_a^{(k)} \leftarrow \text{CrossAttn}(\mathbf{g}_a^{(k)}, \pi_{c_{a \rightarrow b}^{(k+1)}}(\mathbf{g}_b^{(k)}))$
 $\Delta \mathbf{g}_b^{(k)} \leftarrow \text{CrossAttn}(\mathbf{g}_b^{(k)}, \pi_{c_{a \rightarrow b}^{(k+1)}}(\mathbf{g}_a^{(k)}))$
 $\mathbf{g}_a^{(k+1)} \leftarrow \mathbf{g}_a^{(k)} + \Delta \mathbf{g}_a^{(k)}$
 $\mathbf{g}_b^{(k+1)} \leftarrow \mathbf{g}_b^{(k)} + \Delta \mathbf{g}_b^{(k)}$

Algorithm 2: Multiview BA-T

Input: $\{\mathbf{g}_i^{(k)}\}_{i \in \mathcal{V}}, \{c_{i \rightarrow j}^{(k)}\}_{(i,j) \in \mathcal{E}}, \mathcal{G}(\mathcal{V}, \mathcal{E})$
Output: $\{\mathbf{g}_i^{(k+1)}\}_{i \in \mathcal{V}}, \{c_{i \rightarrow j}^{(k+1)}\}_{(i,j) \in \mathcal{E}}$
// Residual computation for each edge
foreach $(i, j) \in \mathcal{E}$ **do**
 $\tilde{\mathbf{g}}_i^{(k)} \leftarrow \pi_{c_{i \rightarrow j}^{(k)}}(\mathbf{g}_i^{(k)})$
 $\tilde{\mathbf{g}}_j^{(k)} \leftarrow \text{LatentMatch}(\tilde{\mathbf{g}}_i^{(k)}, \mathbf{g}_j^{(k)})$
 $\mathbf{r}_{i \rightarrow j}^{(k)} \leftarrow \text{MLP}(f(\tilde{\mathbf{g}}_j^{(k)}) - f(\tilde{\mathbf{g}}_i^{(k)}))$
// Camera update for each edge
foreach $(i, j) \in \mathcal{E}$ **do**
 $\Delta c_{i \rightarrow j}^{(k)} \leftarrow \text{CrossAttn}(c_{i \rightarrow j}^{(k)}, \mathbf{r}_{i \rightarrow j}^{(k)})$
 $c_{i \rightarrow j}^{(k+1)} \leftarrow c_{i \rightarrow j}^{(k)} + \Delta c_{i \rightarrow j}^{(k)}$
// Geometry update for each view
foreach $i \in \mathcal{V}$ **do**
 $\Delta \mathbf{g}_i^{(k)} \leftarrow \text{CrossAttn}(\mathbf{g}_i^{(k)}, \{\pi_{c_{j \rightarrow i}^{(k+1)}}(\mathbf{g}_j^{(k)})\}_{j:(j,i) \in \mathcal{E}})$
 $\mathbf{g}_i^{(k+1)} \leftarrow \mathbf{g}_i^{(k)} + \Delta \mathbf{g}_i^{(k)}$

Table 6: **Quantitative comparison of 4 view inputs on BundleFusion [8].** BA-T achieves comparable accuracy to prior methods while requiring significantly lower memory and substantially faster inference.

Method	Trans. (m)	Rot. (°)	Rel.	$\delta < 1.25$	Time (ms)	Peak Mem (GB)
MapAny [17]	0.14	29.65	0.36	0.30	62.95	3.42
VGGT [39]	0.06	10.72	0.15	0.79	230.13	5.11
BA-T	<u>0.09</u>	<u>16.39</u>	<u>0.20</u>	<u>0.70</u>	50.62	1.35

For multi-view setting, we train an additional 12 hours on 4-view inputs. We evaluate BA-T on 4-view inputs from BundleFusion [8] (547 4-view samples) and compare it with recent multi-view methods [39, 17]. In this experiment, the four views form a fully connected view graph, where a camera token is defined for every pair of views. The evaluation metrics include absolute trajectory error (Trans.), absolute rotation error (Rot.), median relative depth error (Rel.), $\delta < 1.25$ accuracy, inference time, and peak memory. As shown in table 6, BA-T achieves accuracy comparable to prior methods while being substantially more efficient, using only 39% of the peak memory of MapAnything. These results demonstrate that BA-T scales naturally to the multi-view setting while maintaining strong accuracy and significantly improving computational efficiency. Additional multi-view results are presented in fig. 10.

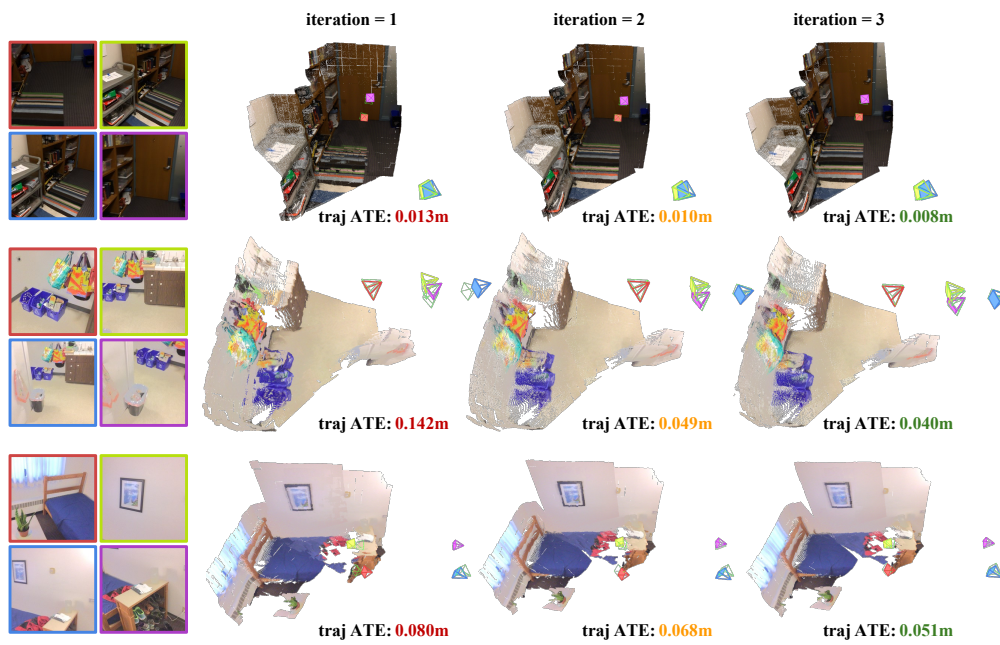


Figure 10: More qualitative 4-view results.